

Gas and Star Formation in the Circinus Galaxy

B.-Q. For^{1,2} \star , B. S. Koribalski³ and T. H. Jarrett⁴

¹*Department of Astronomy, University of Texas, Austin, TX, 78712, USA*

²*ICRAR, University of Western Australia, Crawley, WA, 6009, Australia*

³*Australia Telescope National Facility, CSIRO Astronomy and Space Science, Epping, NSW 1710, Australia*

⁴*Spitzer Science Center, California Institute of Technology, Pasadena, CA, 91125, USA*

Accepted 2012 May 30. Received 2012 May 27; in original form 2012 April 2

ABSTRACT

We present a detailed study of the Circinus Galaxy, investigating its star formation, dust and gas properties both in the inner and outer disk. To achieve this, we obtained high-resolution *Spitzer* mid-infrared images with the IRAC (3.6, 5.8, 4.5, 8.0 μm) and MIPS (24 and 70 μm) instruments and sensitive H I data from the Australia Telescope Compact Array (ATCA) and the 64-m Parkes telescope. These were supplemented by CO maps from the Swedish-ESO Submillimetre Telescope (SEST). Because Circinus is hidden behind the Galactic Plane, we demonstrate the careful removal of foreground stars as well as large- and small-scale Galactic emission from the *Spitzer* images. We derive a visual extinction of $A_V = 2.1$ mag from the Spectral Energy Distribution of the Circinus Galaxy and total stellar and gas masses of $9.5 \times 10^{10} M_\odot$ and $9 \times 10^9 M_\odot$, respectively. Using various wavelength calibrations, we find obscured global star formation rates between 3 and 8 $M_\odot \text{ yr}^{-1}$. Star forming regions in the inner spiral arms of Circinus, which are rich in H I, are beautifully unveiled in the *Spitzer* 8 μm image. The latter is dominated by polycyclic aromatic hydrocarbon (PAH) emission from heated interstellar dust. We find a good correlation between the 8 μm emission in the arms and regions of dense H I gas. The (PAH 8 μm) / 24 μm surface brightness ratio shows significant variations across the disk of Circinus.

Key words: galaxies: individual (Circinus) — galaxies: infrared — galaxies: star formation.

1 INTRODUCTION

The Circinus Galaxy (HIPASS J1413–65), or Circinus in short, is a nearby, highly obscured spiral galaxy which was discovered by Freeman et al. (1977). It is located behind the Galactic Plane ($b \sim -4^\circ$), hidden behind a veil of dust and high star density. Freeman et al. (1977) estimated a Holmberg radius of $\sim 17'$, a morphological type of Sb to Sd and a distance of around 4 Mpc.

Circinus hosts an active galactic nucleus (AGN), superluminous H₂O masers, a recent supernova, a star-forming nuclear ring, a spectacular pair of radio lobes and a gigantic hydrogen disk. In the following we briefly describe these and other features before focusing on the inner disk of Circinus where *Spitzer* data reveal the stellar disk and the onset of two symmetric spiral arms as never seen before.

Matt et al. (1996) show that the X-ray spectrum of Circinus is consistent with Compton scattering and fluorescent emission from cold matter, illuminated by an obscured AGN. Strong far-infrared emission detected

from the nuclear region suggests high starburst activity (Ghosh et al. 1992). Subsequent spectral line observations by Oliva et al. (1994, 1998) confirmed a Seyfert 2 nucleus. The detection of a circum-nuclear ring in the H α line is reported by Marconi et al. (1994) (see also Koribalski 1996; Elmouttie et al. 1998). Circinus also hosts highly variable H₂O megamasers (Gardner & Whiteoak 1982; Whiteoak & Gardner 1986) which appear to arise in the circumnuclear accretion disk and in a low-velocity outflow (McCallum et al. 2009). Bauer et al. (2001) discovered a recent supernova, designated SN1996cr and located just 30'' south of the nucleus of Circinus, and present a multi-wavelength analysis of its lightcurve. High-resolution Australia Telescope Compact Array (ATCA) radio continuum images reveal a prominent pair of linearly polarized radio lobes orthogonal to the disk (Elmouttie et al. 1998; Wilson et al. 2011).

Low-resolution 21-cm observations with the 64-m Parkes radio telescope reveal the enormous H I envelope of the Circinus Galaxy. Its large-scale gas disk extends over an area more than one degree in diameter and is much larger than the stellar disk (Mebold et al. 1976; Freeman et al.

\star E-mail: biqing.for@uwa.edu.au

1977; Henning et al. 2000; Koribalski et al. 2004). ATCA H I observations show in detail the distribution and kinematics of the neutral gas. Circinus has a very extended and significantly warped H I disk with a strong but irregular spiral pattern and an inner bar (Jones et al. 1999; Curran, Koribalski & Bains 2008). Its H I mass, M_{HI} , is $7 \times 10^9 M_{\odot}$ (Freeman et al. 1977; Henning et al. 2000; Koribalski et al. 2004) and its H I diameter is around 100 kpc. It has a Tully-Fisher estimated distance of 4.2 Mpc (Tully et al. 2009). For the analysis to follow, we adopt a distance of $D = 4.2$ Mpc.

The H I physical diameter of the Circinus Galaxy is similar in size to that of the M83 galaxy (Koribalski 2008). While Circinus is relatively isolated and mostly undisturbed, M83 is surrounded by numerous dwarf galaxies, e.g. NGC 5253 (López-Sánchez et al. 2012), and clearly affected by its environment. The tidally distorted outer H I arm and associated debris (close to NGC 5264) as well as a faint stellar stream provide evidence for gas accretion and weak gravitational interactions (Koribalski et al. 2012, in prep.). The large H I disks of Circinus and M83, which are typical for their H I mass (Broeils & van Woerden 1994), allow us to measure their dark matter content out to radii of ~ 50 kpc. High-resolution GALEX images of M83 reveal an extended UV- or XUV-disk, suggesting that star formation is not restricted to the inner stellar disk (Thilker et al. 2005). High-density H I emission is an excellent tracer of star formation in the outer disk of galaxies; good examples are NGC 1512 (Koribalski & López-Sánchez 2009), M83 (Koribalski et al. 2012, in prep.) and Circinus (this paper).

Despite the richness of interesting features in the Circinus Galaxy, most studies have been limited to its nuclear region. While the 2MASS Large Galaxy Atlas (Jarrett et al. 2003) has provided an extensive view of the stellar content of Circinus, the formidable dust opacity at $2 \mu\text{m}$ and the dense stellar foreground prevent a detailed investigation of its large scale and low surface brightness disk. The mid-infrared (MIR) window is ideal to unveil both the old stellar disk population of the obscured Circinus Galaxy as well as the interstellar emission from the new born stars in the outer disk. The high angular resolution ($2''$ in the IRAC $8 \mu\text{m}$ band) and sensitivity of the *Spitzer* telescope makes it more capable than previous infrared observatories (e.g., IRAS, ISO & AKARI). The on-board *Spitzer* high dynamic range IRAC and MIPS imaging instruments allow us to study the full stellar extent of the Circinus disk and the distribution of its warm and cold dust.

The IRAC 3.6 and $4.5 \mu\text{m}$ bands primarily trace the old stellar component in a galaxy while the 5.8 and $8.0 \mu\text{m}$ bands reveal polycyclic aromatic hydrocarbon (PAH) emission from the heated interstellar dust via UV photons radiating from massive young stars. The MIPS $24 \mu\text{m}$ band is dominated by thermal emission from warm ($T > 120$ K) dust inhabiting the molecular and neutral medium phases of the ISM, while the $70 \mu\text{m}$ band traces relatively cold ($T < 50$ K) emitting dust. The relative contribution of the hot dust emission depends on the strength of the radiation field. It has been shown by many semi-empirical dust emission models that an increased radiation field leads to a more rapid increase of the luminosity in the $24 \mu\text{m}$ band than other IR bands (Li & Draine 2001; Draine & Li 2007).

In this paper, we present a detailed study of the Circi-

nus Galaxy, in particular, we focus on its star-forming disk and inner spiral arms. This is the first analysis of Circinus using *Spitzer* images. We compare the mid-infrared images with the gas density of the extended H I disk to unveil star formation sites in the outer disk of Circinus.

The observations and data reduction are presented in Sections 2 and 3. Sections 4–6 describe the derivation of basic parameters via photometry. We derive the stellar and gas masses of Circinus in Section 7. Identification of local star formation sites and global star formation rates using a range of wavelength calibrations are given in Section 8. The relation between PAH $8 \mu\text{m}$ emission and $24 \mu\text{m}$ hot dust emission is explored in Section 9. Finally, a summary and conclusions are given in Section 10.

2 OBSERVATIONS

2.1 *Spitzer* Observations

The mid-infrared imaging observations of the Circinus Galaxy were carried out with the IRAC (3.6, 4.5, 5.8, and $8.0 \mu\text{m}$) and MIPS (24 and $70 \mu\text{m}$) bands of *Spitzer* under the program led by T. Jarrett (PID 50173). The objective was to survey a region large enough to cover the entire H I disk of Circinus, extending well beyond a smaller *Spitzer* survey of the disk (G. Rieke, PID 40936), with a sensitivity to capture the low surface brightness emission in the extended star-forming disk.

For both *Spitzer* instruments, two separate Astronomical Observing Request (AOR) observations (epochs) were combined to improve the sensitivity and to mitigate data artifacts and radiation events.

The IRAC observations consisted of a series of 12 s exposures in high dynamic range mode (HDR) using a 20×19 grid with $154''$ steps (roughly 50% overlap). Including both epochs, the total field coverage is $50' \times 50'$ with a pixel scale of $0''.6$. Each pixel has an exposure depth of roughly two epochs $\times 12 \text{ s} \times$ four coverages, i.e., 96 s per pixel. The achieved 1σ sensitivity in surface brightness is 0.059, 0.045, 0.073 and $0.086 \text{ MJy sr}^{-1}$, respectively, for the 3.6, 4.5, 5.8 and $8.0 \mu\text{m}$ bands. The short-exposure (0.6 s) HDR observations were used to recover the saturated nucleus of Circinus.

The MIPS observations consisted of mapping using the medium scan rate with 21 total scan legs each separated by $148''$. Including both epochs, the total area covered is $\sim 0.9^\circ \times 0.9^\circ$. Each pixel has a depth of coverage or redundancy of roughly 50. The achieved 1σ sensitivity in surface brightness is 0.058 and 1.46 MJy sr^{-1} , respectively, for the 24 and $70 \mu\text{m}$ bands.

We used tools developed by the Spitzer Science Center (SSC) to identify and correct the basic calibrated data (BCD) frame pixels potentially affected by muxbleed (arising from bright stars in the field). After BCD image correction, we used the SSC-developed software package MOPEX to perform background matching, temporal and spatial outlier rejection, astrometric pointing refinement, and co-addition of BCDs into large mosaics for the IRAC and MIPS $24 \mu\text{m}$ observations. In addition to the co-added signal mosaic, the MOPEX products include the uncertainty and coverage maps. For the MIPS $70 \mu\text{m}$ observations, instead of using MOPEX to produce our own mosaics, we combined

both epochs of the SSC-produced post-BCD (PBD) mosaics, which have adequate quality for science analysis.

The achieved angular resolutions are $2''$ for all IRAC bands, $6''$ for the MIPS $24\ \mu\text{m}$ band and $18''$ for the MIPS $70\ \mu\text{m}$ band. We summarize the observing parameters in Table 1 and show the coverage footprints of IRAC and MIPS channels in Figure 1.

2.2 ATCA H I Observations

High-resolution H I observations of the Circinus Galaxy were carried out with the ATCA, located in Narrabri, Australia. Three array configurations (375, 750A and 1.5) were used to obtain single pointings. For details see Jones et al. (1999), who analyze the large-scale H I distribution and kinematics of Circinus at an angular resolution of about $1'$ (rms noise $\sim 1.3\ \text{mJy beam}^{-1}$ per $6.6\ \text{km s}^{-1}$ channel). To study the full H I extent of Circinus, which is much larger than the $33'$ ATCA primary beam, H I mosaic observations were obtained in the 375-m array. For details see Curran, Koribalski & Bains (2008) who analysed both the large-scale H I emission of Circinus (at a resolution of $124'' \times 107'' \times 4\ \text{km s}^{-1}$) as well as the inner CO disk. The latter was observed with the SEST 15-m dish at a resolution of at $45''$ for CO(1–0) and at $22''$ for CO(2–1) and $1.8\ \text{km s}^{-1}$ channel width.

As Circinus lies in the Zone of Avoidance, Galactic H I emission is prominent and detected at radial velocities between about -280 and $+50\ \text{km s}^{-1}$. H I emission from Circinus is observed between $+240$ and $+640\ \text{km s}^{-1}$. Its H I diameter is at least a factor of five larger than the largest estimated optical and infrared diameters.

For the data analysis in this paper we created (1) Galactic H I maps and (2) high-resolution H I maps of the inner disk of the Circinus Galaxy for comparison with the *Spitzer* MIR data. For both tasks we used the MIRIAD software package (Sault, Teuben & Wright 1995).

For the detailed comparison of the *Spitzer* mid-infrared data with the H I data, we need to substantially improve the angular resolution. This can be achieved by robust or uniform weighting of the *uv*-data, i.e. giving more weight to the longest baselines in the array ($\lesssim 6\ \text{km}$). We use the calibrated ATCA *uv*-data from Jones et al. (1999) plus H I data taken in the 6A and 6C array configurations to make H I cubes of the inner Circinus disk at an angular resolution of $15''$. At this resolution, achieved with robust = 0 weighting, good signal-to-noise and high image fidelity was obtained.

To estimate the foreground emission, most prominent in the *Spitzer* IRAC $8\ \mu\text{m}$ and MIPS $24\ \mu\text{m}$ images, we obtained Galactic H I maps of the area using *uv*-data from (a) the high-resolution single-pointing data by Jones et al. (1999) and (b) the low-resolution ATCA mosaic by Curran, Koribalski & Bains (2008). The latter was combined with the stray-radiation corrected H I data from the Galactic All-Sky Survey (GASS; McClure-Griffiths et al. 2009; Kalberla et al. 2010) to estimate the large-scale diffuse Galactic H I emission. After successful subtraction of the scaled Galactic H I map from the *Spitzer* images, some small-scale features remain. Investigation of the Galactic H I emission at high resolution revealed a clear correlation be-

tween the small-scale structure and Galactic H I emission over a specific velocity range (see Section 3.2 for details).

3 DATA REDUCTION

3.1 *Spitzer* Images

The location of the Circinus Galaxy, obscured by the Galactic Plane, presents a challenge for source characterization. In order to determine its global properties, including its shape, size and photometric properties, as well as study its extended low surface brightness star-forming disk, the foreground Milky Way (MW) stars and Galactic ISM emission must first be identified and subtracted from the *Spitzer* images. Figure 2 shows the reduced IRAC and MIPS images with the Circinus Galaxy at the center, obscured by thousands of stars and wide-spread dust emission from the Galactic Plane.

To identify and subtract MW stars, we used detection and characterization tools that were designed for the multi-band imaging observations obtained with the *Spitzer* and WISE space-borne infrared telescopes, developed by the WISE Science Data Center (WSDC) of the Infrared Processing and Analysis Center (IPAC). The distinguishing characteristic of these systems is that they use all bands simultaneously to detect and characterize sources. The detection system is described in Marsh & Jarrett (2012) and the source characterization system in Jarrett et al. (2012) and Cutri et al. (2011). For the Circinus observations, we detect $\sim 90,000$ sources, dominated by the IRAC 3.6 and $4.5\ \mu\text{m}$ sensitivity to Galactic stars. Not all of these detections are of Galactic origin, many are indeed associated with the Circinus Galaxy. In order to mitigate removal of real emission associated with Circinus, we visually inspected the images, taking special notice of detected sources that were either in close proximity to Circinus spiral arms, or were spatially resolved, or had very red colors: those with colors or spatial properties that were more consistent with association to Circinus rather with the Galactic foreground population, were not removed from the images. Using the WISE source characterization system, the surviving Galactic population was then subtracted from the images using the individual IRAC or MIPS point spread function (PSF) to fit the stellar profiles. The resulting images have their MW stellar component removed.

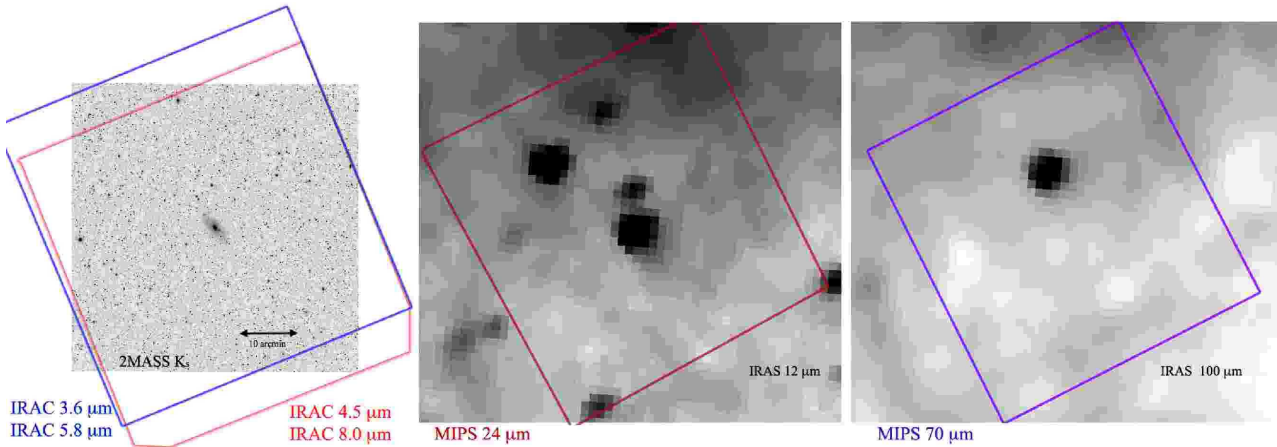
3.2 Galactic ISM Subtraction

The thermal dust emission in the near-IR is caused by a mixture of large and small grains, which dominate the total dust mass of a galaxy. Here we compare the spatial distribution of dust emission, derived from *Spitzer* MIR maps, to that of the H I gas. By conducting a correlation analysis, we aim to separate Galactic from extragalactic (Circinus Galaxy) infrared emission. Specifically, we use single dish and interferometric 21-cm H I data towards the Circinus Galaxy to correct for the Galactic foreground emission present in IRAC $8\ \mu\text{m}$ and MIPS $24\ \mu\text{m}$ images (note that the foreground ISM contribution is negligible in the short-wavelength bands of IRAC).

We employed the ATCA H I data sets of the Circinus Galaxy described by Jones et al. (1999) and

Table 1. *Spitzer* Observing Parameters for the Circinus Galaxy.

| | | |
|--|---|--------------|
| observing dates and pointing positions: | 20 March 2009, 14 ^h 13 ^m 10 ^s , −65° 20′ 21″ 26–27 March 2009, 14 ^h 13 ^m 14 ^s , −65° 21′ 30″ | |
| | IRAC | MIPS |
| coverage area | 50′ × 50′ | 54′ × 52′ |
| grid size | 19 × 20 | 21 scan legs |
| spacecraft orientation | −69° | +30° |
| bands (μm) | 3.6, 4.5, 5.8, 8.0 | 24, 70 |
| total exposure time per pixel | 96 s | ~50 depth |
| 1σ surface brightness limits (MJy sr ^{−1}) | 0.059, 0.045, 0.073, 0.086 | 0.058, 1.46 |

**Figure 1.** *Spitzer* AOR mapping footprints. The first panel shows the IRAC footprints overlaid on a 2MASS K_s -band image. The 2nd panel shows the MIPS-24 map, overlaid on the IRAS 12 μm image, and the third panel shows the MIPS-70 map overlaying the IRAS 100 μm image. The field of view for each panel is about $1^\circ \times 1^\circ$, with North pointing up and East pointing to the left.

Curran, Koribalski & Bains (2008) (see Section 2.2) as well as Parkes H I maps from the Galactic All-Sky Survey (GASS). The velocity range and resolution of these H I data sets allow a clear separation and analysis of both the Galactic features and the extended structure of the Circinus Galaxy.

The high-resolution *Spitzer* images (see Figure 2) show structures on all scales. While the IRAC 3.6, 4.5, and 5.8 μm images are dominated by scores of foreground stars, and diffuse foreground emission (filaments, bubbles, sheets, etc.) is pervasive in the IRAC 8 μm and MIPS 24 μm images. By combining the Parkes and ATCA H I data towards Circinus over the Galactic velocity range, we constructed a high angular resolution image that matches the large-scale MIR features.

3.2.1 Subtracting the Large-scale Galactic Foreground

We made ATCA H I mosaic images of the Galactic H I emission (over the velocity range from −220 to +220 km s^{−1}) by Fourier transforming the data obtained by Curran, Koribalski & Bains (2008) supplemented by H I data taken with the very compact H75 array. The resulting ATCA data cube has a velocity resolution of 4 km s^{−1} and an angular resolution of 1′.

The Parkes H I data were retrieved from the GASS data

2 release website¹ and is corrected for stray radiation and radio frequency interference (Kalberla et al. 2010). GASS covers the region south of $\delta = +1^\circ$ in the Local Standard of Rest (LSR) velocity range from −400 to +500 km s^{−1}, with 1 km s^{−1} velocity resolution and an angular resolution of 16′.

To combine the interferometer (ATCA) and single-dish (Parkes) data, we explore two methods: (a) merging in the Fourier domain (linear method) and (b) merging during deconvolution (non-linear method) (see Stanimirovic 2002). For both methods, the GASS data were converted from Kelvin to Jy beam^{−1}, and from LSR to the barycentric (heliocentric) velocity reference frame, then regridded to match the ATCA mosaic pixel scale and velocity channels. We applied the residual primary beam attenuation (a gain function) present in the ATCA mosaic to the GASS data prior to combining them.

To generate the residual image, a deconvolved and restored ATCA mosaic is needed. We first applied the mosaic Steer CLEAN algorithm (Steer, Dewdney & Ito 1984) to deconvolve the image, but ultimately failed due to its limitation in handling diffuse emission. In its place, we employed a maximum-entropy based deconvolution algorithm (MOSMEM), which we found to work better on diffuse emission. The only drawback is that MOSMEM does not handle

¹ <http://www.astro.uni-bonn.de/hisurvey/gass>

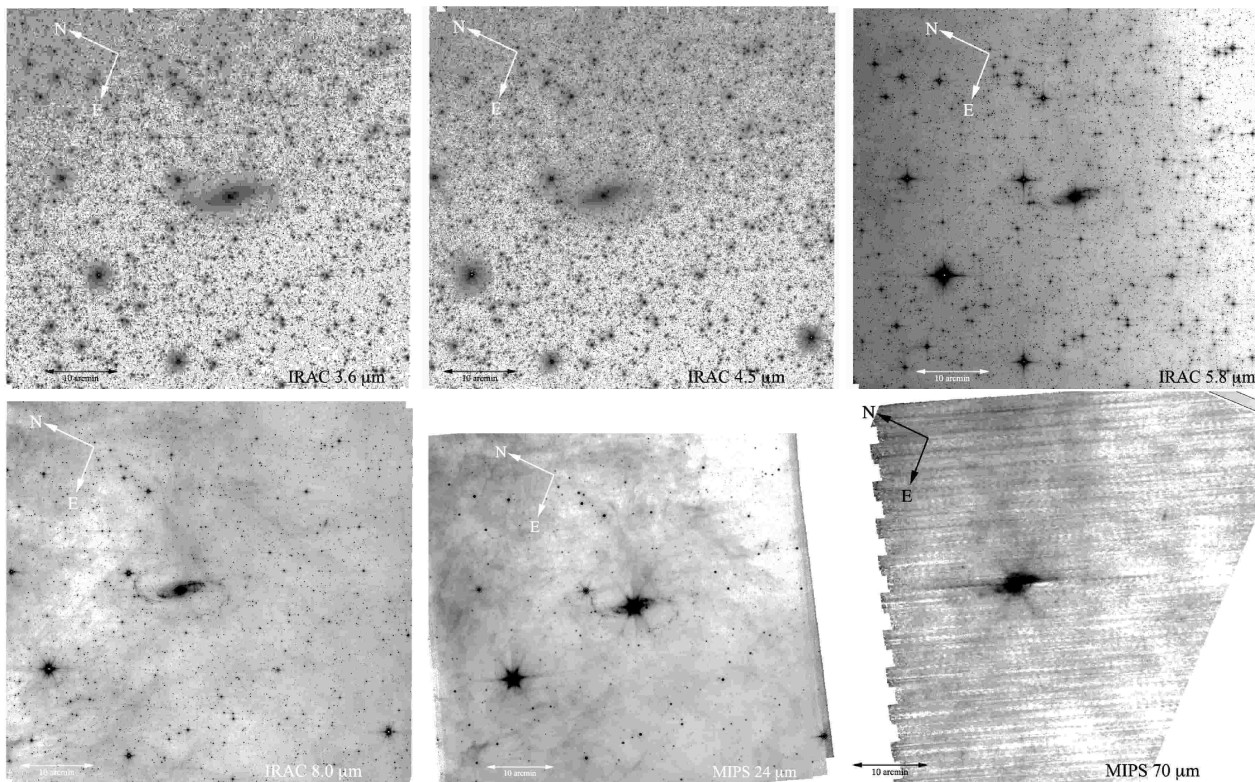


Figure 2. *Spitzer* 3.4 to 70 μm images of the Circinus Galaxy. The observed field of view is nearly one degree across. The image orientation corresponds to the original spacecraft rotation angle at the time of the observations. The North and East directions are indicated by arrows, and a 10' scale bar is given at the bottom left.

negative features. Subsequently, an integrated H I map was created using all channels with Galactic H I emission (velocities ranging from -88 to $+124$ km s^{-1}). The rms achieved is around 4.5 mJy beam^{-1} . Around 93% of the total H I flux was recovered in the combined Galactic map as compared to the single-dish data alone. Figure 3 illustrates the transformation of the individual maps to the combined result.

The procedure for subtracting the Galactic foreground from the *Spitzer* images was as follows: —(a) A constant was added to the calibrated IRAC 8 μm and MIPS 24 μm images to account for some over-subtraction of the background during mosaic construction. The offset was determined based on the post-BCD mosaics delivered by SSC, where the background had not been subtracted. —(b) The resulting *Spitzer* images were then divided by the integrated Galactic H I emission map to determine the respective correlation factors. —(c) We then subtracted the scaled integrated Galactic H I emission maps from the *Spitzer* images produced in step (a). —(d) A residual smooth gradient over the full IRAC 5.8 μm and 8 μm images, known as the “first frame effect” (IRAC Instrument Handbook) was fitted and removed using a first order polynomial (after masking the Circinus Galaxy and another background galaxy).

In Figure 4 we show the IRAC 8 μm image before and after foreground subtraction. The H I contours trace a range of structures, much of which correlate well with the infrared dust emission. In particular, the Parkes H I data combined with the ATCA H I mosaic allow us to match and subtract the diffuse foreground emission on large scales. Some small-scale structure remains, most noticeably the “spur” struc-

ture to the west and overlaying the southwest disk of Circinus. It was recently pointed out that the MIR PAH emission of M 83, associated with current star formation, was highly correlated with dense ($n > 10^2$ cm^{-3}) H I emission (Jarrett et al. 2012). It likely that the dense filamentary components of the Galactic ISM will also be correlated with the MIR PAH emission. Isolating the dense H I gas is the key to identifying and removing the “spur” contaminant from the *Spitzer* imaging. The removal of this filament is described in the next subsection.

3.3 The Galactic Spur

We re-analyzed single pointing 21-cm data of the Circinus Galaxy taken by Jones et al. (1999) with three configurations of the ATCA (see Section 2.2). In addition to the detailed H I studies of Circinus itself, these data allowed us to make high-resolution maps of the Galactic H I emission. Our aims are (a) to map the Galactic H I emission and search for features matching PAH structures as seen in the *Spitzer* IRAC 8 μm and MIPS 24 μm images and (b) to map the distribution and dynamics of the high density H I gas in the inner disk of the Circinus Galaxy.

We Fourier-transformed the *uv*-data from all three configurations to image the Galactic H I emission over a velocity range from -220 to $+220$ km s^{-1} and at a range of angular resolutions. Using robust = 0 weighting, which resulted in an angular resolution of $\sim 35''$, we were able to identify the Galactic spur at velocities ranging from about -50 to -30 km s^{-1} . Using the primary beam corrected H I data

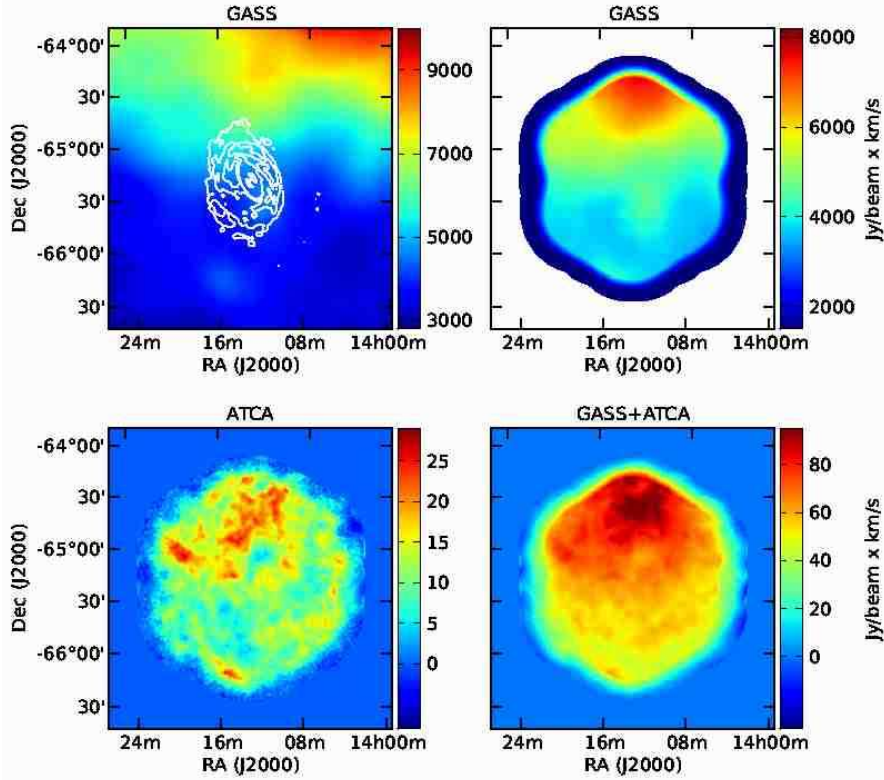


Figure 3. Galactic H I emission in the direction of the Circinus Galaxy. **Top:** We show the integrated Galactic H I distribution as obtained from the Parkes H I data (left) and tapered with the gain function of the ATCA H I mosaic (right). For comparison we overlay the large-scale H I distribution (white contours) of the Circinus Galaxy; the contour levels are 0.5, 3.0 and 6.0 Jy beam⁻¹ km s⁻¹. **Bottom:** We show the integrated Galactic H I distribution as obtained from the ATCA H I mosaic observations (left) and the combined Parkes and ATCA H I data set (right). The latter is used to remove the large-scale Galactic foreground emission from the *Spitzer* IRAC 8 μ m and MIPS 24 μ m images.

cube, we created moment maps of the feature (see Figure 5). It is a large filamentary structure, spanning diagonally across the Circinus field, intersecting the southwestern disk of the galaxy. The bulk of the structure has a mean velocity of -45 km s^{-1} , while further to the southwest, another adjoining gas cloud appears at a velocity of -35 km s^{-1} . The shape and intensity of the H I spur is largely correlated with the 8 μ m PAH (see Figure 5), which we determine to be a scaling factor ~ 0.8 . Accordingly, the H I distribution of the spur, scaled by this factor, was subtracted from the IRAC 8 μ m image. A reasonable subtraction was achieved as Circinus remained symmetric and undistorted, thus allowing a much improved view of the star-forming inner spiral arms of the Circinus Galaxy. Figure 6 illustrates the process. We are reasonably confident that the observed spur is a Galactic feature and not associated with the Circinus Galaxy itself.

Following the analysis of H I emission and absorption line measurements towards the pulsar PSR 1401–6357 (Johnston et al. 1996), we can assign an approximate distance to the Galactic spur. A velocity of -50 km s^{-1} corresponds to the tangent point in that direction and a distance of $\sim 5 \text{ kpc}$. The integrated H I flux density of the spur is $\sim 140 \text{ Jy km s}^{-1}$, corresponding to an H I mass of $\sim 10^3 M_{\odot}$, and size of $\sim 20' (30 \text{ pc})$.

In the remaining analysis, we use the stellar and

Galactic-ISM subtracted imaging to measure and characterize the Circinus galaxy.

4 SURFACE BRIGHTNESS PROFILES

We obtain the surface photometry of Circinus by fitting elliptical apertures to the *Spitzer* images in all IRAC bands and the MIPS 24 μ m and 70 μ m bands. The measurements were performed for radii from $10''$ to $600''$, in steps of $10''$, assuming a position angle of $PA = 210^\circ$ and an inclination angle of $i = 65^\circ$ (Curran, Koribalski & Bains 2008).

The surface brightness (*SB*) profile, in units of mag arcsec⁻², can be represented by

$$SB = -2.5 \log_{10} \left(\frac{f_A \times F \times C}{F_0} \right), \quad (1)$$

where f_A is an effective aperture correction factor to account for extended emission from the IRAC PSF and from the diffuse scattering of the emission across the IRAC focal plane, F is the inclination-corrected flux density in units of MJy sr^{-1} , C is a conversion factor, $2.35 \times 10^{-5} \text{ Jy arcsec}^{-2}$, and F_0 is the zero-magnitude flux of the star Vega. We used $f_A = 0.944, 0.937, 0.772, 0.737$ and $F_0 = 280.9 \pm 4.1, 179.7 \pm 2.6, 115.0 \pm 1.7, 64.13 \pm 0.94 \text{ Jy}$ for the corresponding IRAC channels 1, 2, 3, 4 from Reach et al. (2005). For the MIPS 24 μ m and 70 μ m bands no aperture correction

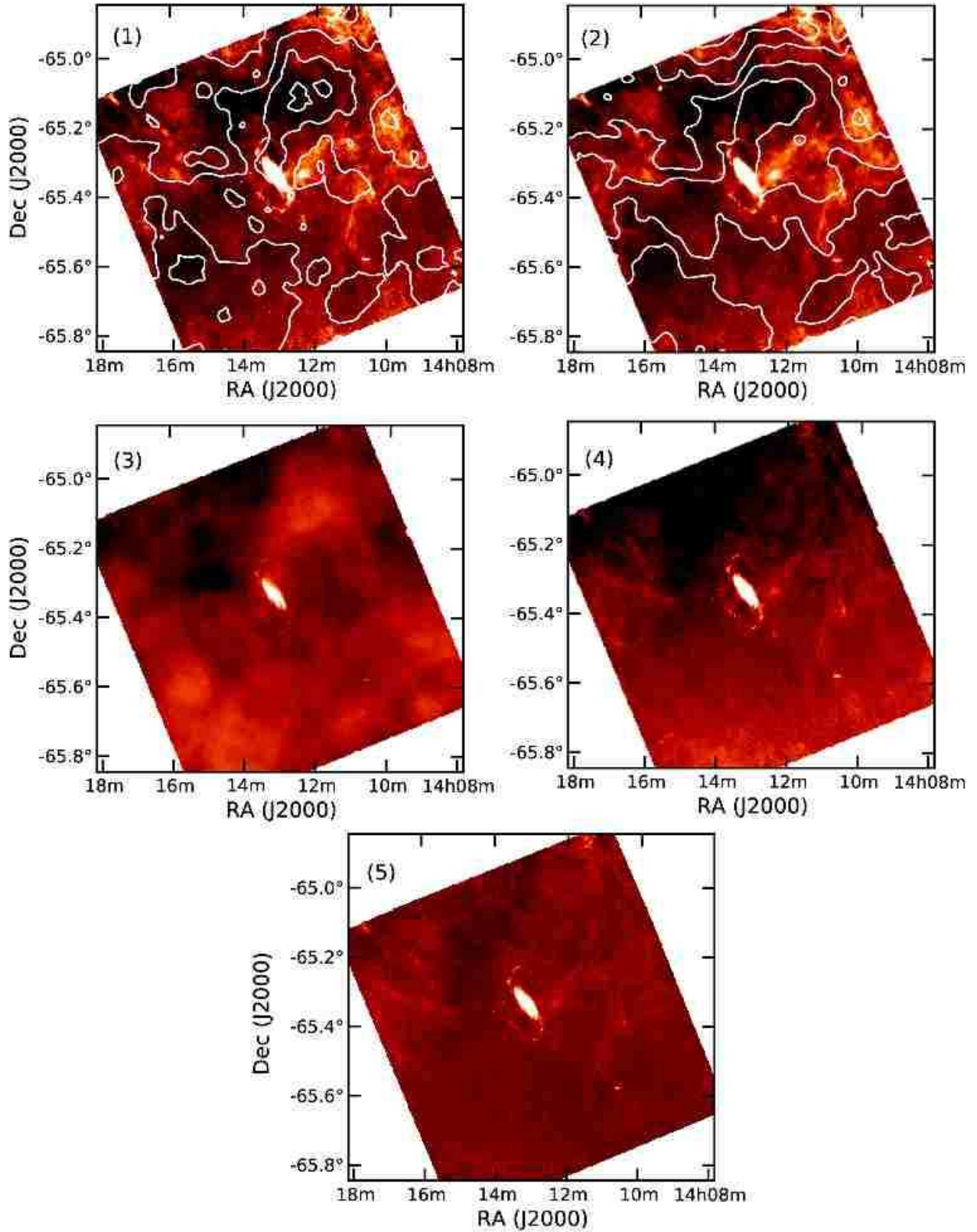


Figure 4. *Spitzer* IRAC 8 μm images of the Circinus Galaxy and surroundings after the removal of foreground stars and Galactic emission. White contours indicate the Galactic H I emission as obtained from the ATCA mosaic observations (panel 1) and the combined Parkes and ATCA data (panel 2). The results of subtracting the scaled Galactic H I emission from the 8 μm image are shown in panels (3) and (4), respectively. After removing the smooth gradient from the panel 4 result, we obtain a much cleaner IRAC 8 μm image of Circinus (panel 5).

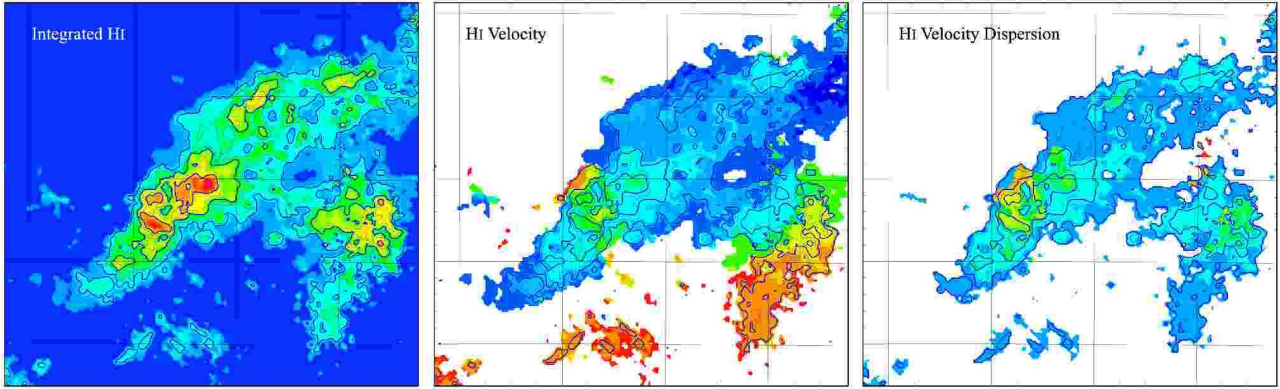


Figure 5. High resolution ATCA H I integrated and velocity distribution of the Galactic foreground to the Circinus Galaxy. The velocity ranges between -50 to -30 km s^{-1} . **Left:** Integrated H I distribution (0th moment). **Middle:** Mean H I velocity field (1st. moment). The main feature (blue) has velocities around -45 km s^{-1} , while the small SW cloud (orange) has velocities around -35 km s^{-1} . **Right:** Mean H I velocity dispersion (2nd. moment) with maximum velocities around 7 km s^{-1} .

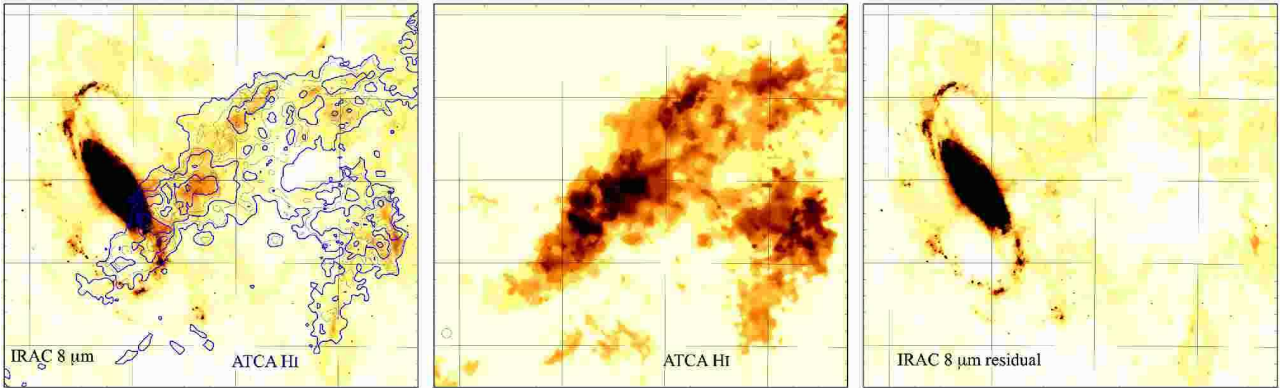


Figure 6. *Spitzer* IRAC $8\text{ }\mu\text{m}$ imaging of the Circinus Galaxy and the Galactic foreground as traced in ATCA H I maps at high angular resolution. **Left:** IRAC $8\text{ }\mu\text{m}$ image with large-scale Galactic emission removed (for details see Section 3.2.1), overlaid with ATCA H I contours of the Galactic spur. The contour levels are $0.2, 0.3, 0.4, 0.5$ and 0.6 $\text{Jy beam}^{-1} \text{ km s}^{-1}$; the first contour corresponds to an H I column density of $1.8 \times 10^{20} \text{ cm}^{-2}$. **Middle:** ATCA H I distribution of the Galactic spur. The spur was identified in the H I spectral cube, velocities between -50 and -30 km s^{-1} (see Fig. 5). The synthesized beam of $\sim 35''$ is indicated at the bottom left. **Right:** IRAC $8\text{ }\mu\text{m}$ image with the Galactic spur removed from the mid-infrared emission. The coordinate grid is in steps of $5'$ in Dec and $1''$ in RA.

is needed, and we use $F_0 = 7.17$ Jy and 0.778 Jy, respectively. Table 2 lists our measured radial flux densities and radial surface brightness densities for the Circinus Galaxy. Figure 7 shows the *SB* profiles of Circinus as obtained in five *Spitzer* bands as well as the 2MASS *J*, *H*, and *K_s* bands from Jarrett et al. (2003).

5 PHOTOMETRY

We performed basic photometry and source characterization of the Circinus Galaxy by using the pipeline developed for the 2MASS Large Galaxy Atlas (Jarrett et al. 2003) and updated for the WISE High Resolution Galaxy Atlas (Jarrett et al. 2012). The pipeline provides an interactive system to identify foreground (contaminant) stars and assists in shape/extent characterization, surface brightness and integrated flux measurements. The user specifies the initial shape parameters, including the annulus used to estimate the local background and the elliptical aperture for source measurements. For each band, the local background is de-

termined from the mode of the pixel value distribution, a robust metric for the “sky”, and thus is adopted as the local background value.

The shape of the galaxy is determined using the 3σ elliptical isophote, while the size or extent of the visible galaxy corresponds to the 1σ isophote. The isophotal fluxes correspond to the integral of the elliptical shape defined by the axis ratio, position angle and isophotal radius. Additionally, in order to compare fluxes across bands to derive colors, we adopt the IRAC $8\text{ }\mu\text{m}$ aperture as the fiducial aperture for all IRAC measurements (whereas the MIPS $24\text{ }\mu\text{m}$ and $70\text{ }\mu\text{m}$ measurements are derived from their own isophotal apertures). Finally, the azimuthal elliptical-radial surface brightness is then characterized using a double Sérsic function, where one component is fit to the inner region (i.e., the bulge) of the galaxy and the second component is fit to the outer region (i.e., the disk). The fit to the radial surface brightness is used to estimate the total flux by extrapolating the fit to larger radii, corresponding to three times the disk scale length beyond the isophotal radius. This threshold rep-

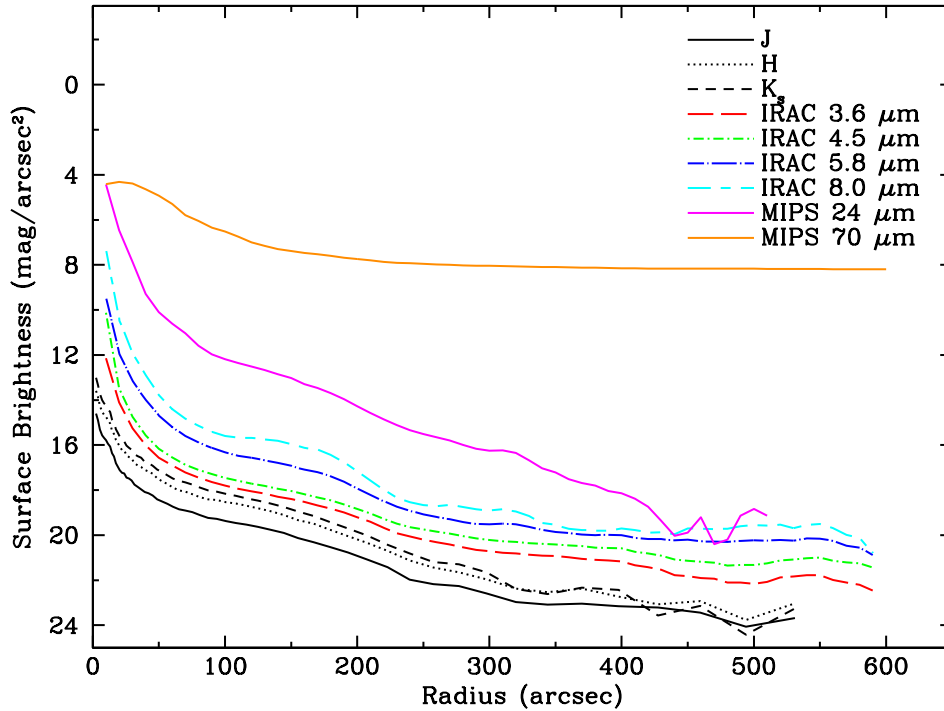


Figure 7. Inclination-corrected surface brightness (cSB) profiles of the Circinus Galaxy in all four IRAC bands, the MIPS 24 μm and 70 μm bands, and the 2MASS J , H , and K_s bands. See Table 2 for details; no extinction correction has been applied.

resents a practical balance between capturing the outer disk light and mitigating fit errors that accumulate with radius.

The source characterization results are as follows. The central position is determined to be RA (J2000) = 213.29130°, Dec (J2000) = −65.33926°. The 3σ isophote shape is an ellipse with axis ratio $b/a = 0.485$ (ie. an inclination angle of $\sim 63^\circ$) at a position angle of $PA = 28.4^\circ$ (208.4°). The size of the galaxy based on the 1σ (fiducial) isophote radius is $R_{\text{iso}} = 603''.5$ (20.1' in diameter). Using these parameters, we determine the integrated flux density, F_λ , in all MIR bands. Note that for the case of MIPS-70, an additional color correction is required to account for the spectral differences between Circinus (whose MIR spectrum has a power-law spectral index of -2) and the MIPS calibrators. The color correction, or scaling factor, is 1.09 (see the MIPS Instrument Handbook).

The results of the Circinus photometry are summarized in Table 3. The photometric uncertainty incorporates the formal (Poisson) errors as well as the estimated background uncertainty. However, given that a significant foreground stellar population was removed from the images (notably for 3.6 and 4.5 μm), and at longer wavelengths the Galactic ISM subtraction was a significant operation, the quoted uncertainties are likely to be too generous and thus represent a lower limit.

6 REDDENING AND SPECTRAL ENERGY DISTRIBUTION

Dust reddening affects the measured fluxes and is particularly severe for the Circinus Galaxy. A common method

for estimating the reddening relies on the all-sky extinction map of Schlegel, Finkbeiner & Davis (1998a), which is based on the *Infrared Astronomical Satellite* (IRAS), and *Diffuse Infrared Background Experiment* (DIRBE) measurements of IR dust emission. However, this map is inaccurate in high dust column density area and uncalibrated for $|b| < 5^\circ$; it also tends to overestimate the reddening in regions of high extinction (see e.g., Arce & Goodman 1999). A higher spatial resolution all-sky dust emission map is needed to solve the problem of estimating the reddening in high extinction regions. A recent study by Kohyama et al. (2010) has proposed a new method to construct a high spatial resolution extinction map but it is currently limited to the Cygnus region.

Another way to derive the dust extinction towards Circinus is by comparing its near-IR (NIR) and MIR Spectral Energy Distribution (SED) to galaxy model templates with different values of A_V . The model templates were obtained from the SWIRE library (Polletta et al. 2007), the majority of which were generated from the GRASIL code (Silva et al. 1998).

In order to obtain the Circinus SED with various A_V values, we adopt the wavelength-dependent extinction law of Cardelli, Clayton & Mathis (1989):

$$A_\lambda/A_V = a(x) + b(x)/R_V, \quad (2)$$

where $a(x) = 0.574x^{1.61}$, $b(x) = -0.527x^{1.61}$, $x = 1/\lambda$ in μm^{-1} , and $R_V = 3.1$ for broadband filters. This relation was used to calculate the intrinsic magnitude, defined as $M_{\text{Intrinsic}} = M_{\text{observed}} - A_\lambda$, and then converted to flux with $F_\nu = F_0 \times 10^{-0.4M_{\text{Intrinsic}}}$. The zero-magnitude flux, F_0 , of

| Radius ($''$) (1) | $F_{3.6\mu\text{m}}$ (MJy sr $^{-1}$) (2) | rms (3) | cSB (mag/($''$) 2) (4) | $F_{4.5\mu\text{m}}$ (MJy sr $^{-1}$) (5) | rms (6) | cSB (mag/($''$) 2) (7) | $F_{5.8\mu\text{m}}$ (MJy sr $^{-1}$) (8) | rms (9) | cSB (mag/($''$) 2) (10) | $F_{8.0\mu\text{m}}$ (MJy sr $^{-1}$) (11) | rms (12) | cSB (mag/($''$) 2) (13) | $F_{24.0\mu\text{m}}$ (MJy sr $^{-1}$) (14) | rms (15) | cSB (mag/($''$) 2) (16) | $F_{70.0\mu\text{m}}$ (MJy sr $^{-1}$) (17) | rms (18) | cSB (mag/($''$) 2) (19) |
|---------------------------|--|------------|--------------------------------------|--|------------|--------------------------------------|--|------------|---------------------------------------|---|-------------|---------------------------------------|--|-------------|---------------------------------------|--|-------------|---------------------------------------|
| 10 | 418.48 | 798.70 | 12.14 | 1289.33 | 3107.21 | 10.44 | 1791.66 | 3262.49 | 9.81 | 9710.94 | 16982.44 | 7.39 | 12234.36 | 12432.62 | 4.43 | 1332.25 | 331.76 | 4.42 |
| 20 | 68.84 | 41.95 | 14.10 | 58.98 | 47.21 | 13.79 | 187.16 | 108.67 | 12.26 | 562.44 | 796.98 | 10.48 | 1884.21 | 2029.40 | 6.46 | 1470.84 | 757.50 | 4.32 |
| 30 | 23.89 | 13.64 | 15.25 | 18.32 | 11.90 | 15.06 | 61.18 | 35.09 | 13.47 | 146.61 | 95.55 | 11.94 | 514.92 | 664.68 | 7.87 | 1379.43 | 1100.25 | 4.39 |
| 40 | 11.79 | 4.76 | 16.01 | 8.63 | 4.19 | 15.87 | 28.21 | 14.93 | 14.31 | 60.26 | 36.95 | 12.91 | 138.81 | 145.15 | 9.29 | 1091.89 | 1001.56 | 4.64 |
| 50 | 7.07 | 2.36 | 16.57 | 4.95 | 1.95 | 16.48 | 14.94 | 8.39 | 15.00 | 26.54 | 17.62 | 13.80 | 66.10 | 53.09 | 10.10 | 834.47 | 860.51 | 4.93 |
| 60 | 5.14 | 1.77 | 16.91 | 3.50 | 1.26 | 16.85 | 9.23 | 4.41 | 15.53 | 14.95 | 8.82 | 14.42 | 41.26 | 33.90 | 10.61 | 600.75 | 651.90 | 5.29 |

Notes: Table 2 is published in its entirety in the electronic edition of the *MNRAS*. A portion is shown here for guidance regarding its form and content.

Table 3. *Spitzer* photometry results of the Circinus Galaxy.

| Flux density | [Jy] | [mag] |
|----------------------|------------------|------------------|
| $F_{3.6\mu\text{m}}$ | 6.78 ± 0.12 | 4.04 ± 0.02 |
| $F_{4.5\mu\text{m}}$ | 7.81 ± 0.15 | 3.41 ± 0.02 |
| $F_{5.8\mu\text{m}}$ | 14.78 ± 0.28 | 2.23 ± 0.02 |
| $F_{8.0\mu\text{m}}$ | 47.82 ± 0.91 | 0.32 ± 0.02 |
| $F_{24\mu\text{m}}$ | 79.65 ± 1.49 | -2.61 ± 0.02 |
| $F_{70\mu\text{m}}$ | 280.0 ± 4.9 | -6.38 ± 0.02 |

Notes: The MIPS-70 integrated flux was measured using a circular aperture of radius 10 arcmin. The flux was then color corrected with a scaling factor of 1.09, appropriate for a steeply rising MIR spectrum, as specified in the MIPS Instrument Handbook,

Vega (see Section 4) is 1594.0, 1024.0, and 666.7 Jy for J , H , and K_s bands, respectively. The shift from observed to rest wavelength is negligible at the redshift of Circinus ($z = 0.00145$). We then fit the Circinus SED with various values of A_V to the best represented Seyfert 2 model template. The template was normalized to the 2MASS J -band value. We derive a visual extinction of $A_V = 2.1 \pm 0.4$ mag. Comparing our value to the $A_B = 6.276$ and $A_V = 4.694$ from Schlegel, Finkbeiner & Davis (1998b), we confirm the previous finding of over-estimation based on the current all-sky extinction map in high column density region.

In Figure 8 we show the constructed Circinus SED using 2MASS J , H , and K_s values (Jarrett et al. 2003), and our IRAC and MIPS measurements (black dots). For comparison, we include the high-resolution ISO-SWS spectrum (magenta) of the nuclear and circumnuclear regions of Circinus (Moorwood et al. 1996). The spectrum contains a number of high excitation ionic and molecular emission lines that arise from the strong radiation field that is sustained by the AGN. Representing a composite of AGN and star formation features, the spectral components that dominate the broadband photometric measurements, are the PAH bands at 6.2, 7.7, 8.6 and 11.3 μm , deep silicate absorption at 10 μm , and the steeply rising continuum. Model templates are fit and normalized to the near-infrared, including the a Seyfert 2 (red) and Seyfert 1.8 model templates (green), as well as old stellar population, elliptical galaxy model template (blue) to trace the host stellar light. The NIR region of the SED is dominated by the bulge population while the MIR region is dominated by the molecular and dust components of the Circinus ISM. We summarize our results in Table 4.

7 MASSES

The total mass of a galaxy consists of the visible stellar, dust and gas masses as well as dark matter. In the following subsections, we derive the visible mass components of the Circinus Galaxy.

7.1 Stellar Mass

The IRAC 3.6 and 4.5 μm bands primarily trace the stellar light in the disk and bulge of a galaxy. We represent the stellar mass surface density with

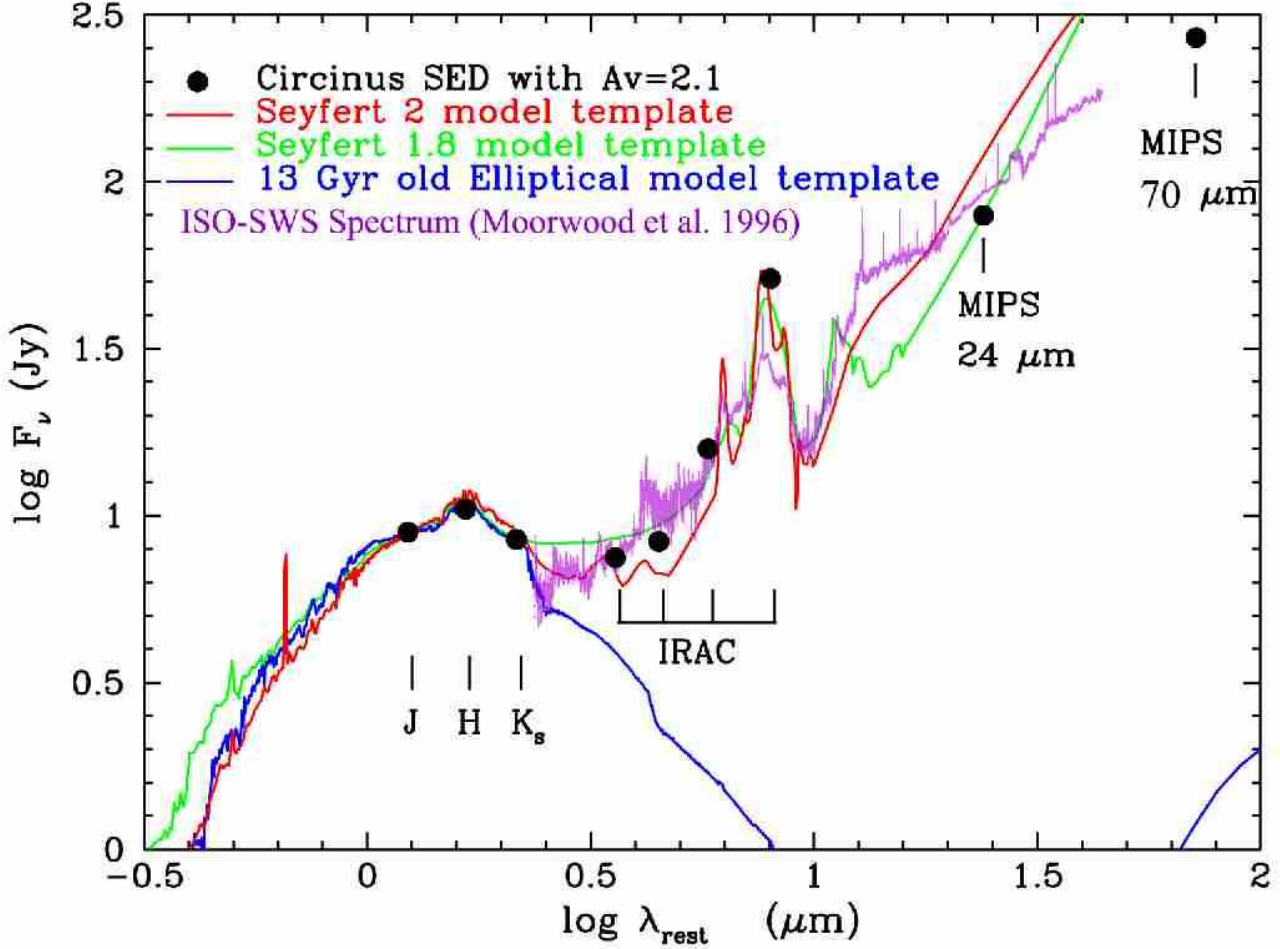


Figure 8. The Circinus SED with 2MASS J , H , K_s band fluxes from the Large Galaxy Atlas (Jarrett et al. 2003) and MIR measurements from the IRAC and MIPS bands. Overlaid in magenta is the high resolution ISO-SWS spectrum of the central region of Circinus (Moorwood et al. 1996). The galaxy model templates are retrieved from the SWIRE library (Polletta et al. 2007) and normalized to the 2MASS J -band value. We derive a visual extinction of $A_V = 2.1$ mag.

Table 4. Extinction-corrected total magnitudes ($M_{\text{Intrinsic}}$), fluxes (F_ν) and spectral luminosities (νL_ν) in different NIR and MIR bands for the Circinus Galaxy. The extinction, A_λ , is calculated using Eq 2 and $A_V = 2.1$ mag.

| λ_{rest} (μm) | A_λ (mag) | $M_{\text{Intrinsic}}$ (mag) | F_ν (Jy) | νL_ν ($10^9 L_\odot$) |
|--|----------------------|---------------------------------|-----------------|-----------------------------------|
| 1.233 | 0.605 | 5.63 | 8.92 | 11.90 |
| 1.660 | 0.376 | 4.98 | 10.46 | 10.39 |
| 2.156 | 0.246 | 4.74 | 8.49 | 6.49 |
| 3.595 | 0.107 | 3.94 | 7.49 | 3.43 |
| 4.493 | 0.076 | 3.33 | 8.37 | 3.07 |
| 5.792 | 0.076 | 2.15 | 15.85 | 4.51 |
| 7.988 | 0.076 | 0.24 | 51.25 | 10.58 |
| 23.965 | 0.000 | -2.61 | 79.35 | 5.46 |
| 71.42 | 0.000 | -6.38 | 280.0 | 6.51 |

$$\Sigma_*(r) = C_\lambda \Upsilon_\lambda f_{A,\lambda} \frac{F(r)}{F_0} \cos i, \quad (3)$$

where C_λ is the conversion factor for the corresponding wavelength bands ($C_{3.6\mu\text{m}} = 0.196 M_\odot \text{pc}^{-2}$ and $C_{4.5\mu\text{m}} =$

$0.201 M_\odot \text{pc}^{-2}$; Oh et al. 2008), Υ_λ is the mass-to-light ratio in solar unit, $F(r)$ is the inclination-corrected flux density in Jy, $f_{A,\lambda}$ is the aperture correction factor and F_0 is the zero-magnitude flux of Vega (the respective values for f_A and F_0 are given in Section 4). The λ index indicates a wavelength dependency for these quantities, which are usually determined within the specific photometric band.

The stellar mass-to-light ratio, Υ_λ , depends on many other physical parameters, such as the initial mass function (IMF), the recent star formation history of the galaxy, etc. Determining Υ_λ , optically was difficult until a study by Bell & de Jong (2001), who found a strong correlation between the stellar mass-to-light ratio and the integrated color of the stellar population. To determine Υ_λ of Circinus in the IRAC bands, we can utilize its color indices.

We adopt Eq. (8) of Westmeier, Braun & Koribalski (2011), which describes the relation between a galaxy's stellar mass-to-light ratio and its 2MASS $J - K_s$ color index. This equation was derived from the relations of Bell & de Jong (2001). To incorporate the global color index of $J - K_s$ to the IRAC bands, we used Eqs. (6) and (7) of Oh et al. (2008), which were derived from the stellar

population synthesis model. The final adopted equations to calculate the stellar mass-to-light ratio in the IRAC 3.6 and 4.5 μm bands are:

$$\Upsilon_{3.6\mu\text{m}} = 0.92 \times 10^{(1.434(J-K_s)-1.380)} - 0.05, \quad (4)$$

$$\Upsilon_{4.5\mu\text{m}} = 0.91 \times 10^{(1.434(J-K_s)-1.380)} - 0.08. \quad (5)$$

Using the extinction corrected J and K_s -band magnitudes (see Table 4), we obtain $\Upsilon_{3.6\mu\text{m}} = 0.679 \pm 0.070$ and $\Upsilon_{4.5\mu\text{m}} = 0.641 \pm 0.060$. We then use Eq. (3) to calculate the radial stellar mass surface density with the flux density of each band. The resulting total stellar mass is $9.5 \times 10^{10} M_\odot$. A summary of the stellar surface mass densities, $\Sigma_*(r)$, is given in Table 5.

7.2 Gas Masses

We derive the radial H I gas mass surface density, $\Sigma_{\text{HI}}(r)$ ($M_\odot \text{ pc}^{-2}$), assuming the same orientation parameters as before ($PA = 210^\circ$ and $i = 65^\circ$), out to a radius of $2000''$. We use

$$\Sigma_{\text{HI}}(r) = m_{\text{H}} N_{\text{HI}}(r) \cos i, \quad (6)$$

where $m_{\text{H}} = 1.674 \times 10^{-27} \text{ kg}$ is the mass of a hydrogen atom and N_{HI} is the H I column density in cm^{-2} . We estimate the H I mass as $M_{\text{HI}} = \Sigma_{\text{HI}}(r) \times \text{area}$, which resulted in $6.6 \times 10^9 M_\odot$. The single-dish estimate of $M_{\text{HI}} = 7 \times 10^9 M_\odot$ (Freeman et al. 1977; Henning et al. 2000; Koribalski et al. 2004) is, as expected, slightly higher.

The distribution of cold molecular hydrogen gas (H_2) in galaxies is difficult to measure directly. A proxy, such as the CO line, is generally used as a tracer. To estimate the H_2 gas mass surface density, Σ_{H_2} , of the inner disk of the Circinus Galaxy we use the CO(1–0) map provided by Curran, Koribalski & Bains (2008). To determine Σ_{H_2} , we first compute the column density via the CO to H_2 conversion factor, X_{CO} . The latter is defined by the ratio of the H_2 column density, N_{H_2} in cm^{-2} , to the integrated CO intensity, I_{CO} in K km s^{-1} . It has been derived using various methods such as the virial mass method (Solomon et al. 1987) and γ -ray emission caused by the collision of cosmic-rays with hydrogen (Bloemen et al. 1986). There appears to be no universal X_{CO} factor as it varies with the metallicity of the galaxy, UV radiation field and cosmic-ray density. Nevertheless, previous studies suggested that X_{CO} is accurate in the Milky Way disk (see Solomon et al. 1987; Hunter et al. 1997). To compare the total molecular gas mass with the study by Curran, Koribalski & Bains (2008), we adopt the same X_{CO} factor of $2.3 \times 10^{20} \text{ cm}^{-2} / (\text{K km s}^{-1})$ (Strong et al. 1988) and a 36% mass correction for Helium, $f_{\text{He}} = 1.36$. We use

$$\Sigma_{\text{H}_2}(r) = 2m_{\text{H}} f_{\text{He}} N_{\text{H}_2}(r) \cos i. \quad (7)$$

The measurements of I_{CO} were carried out from $0''$ to $300''$ (the furthest detection in the CO(1–0) map). For the radial ring estimates we adopt $i = 65^\circ$ and $PA = 214^\circ$. We determine $\Sigma_{\text{H}_2} = 1441 M_\odot \text{ pc}^{-2}$ and derive $M_{\text{H}_2} = 2.1 \times 10^9 M_\odot$.

We calculate a total gas mass, $M_{\text{gas}} = M_{\text{HI}} + M_{\text{H}_2}$, of about $9 \times 10^9 M_\odot$. A summary of the measured gas mass surface density of Circinus is presented in Table 5. Figure 9 shows the stellar and gas masses surface densities as a function of radius.

Table 5. Radial mass surface density of gas and stellar components for the Circinus Galaxy. A position angle of $PA = 210^\circ$ and an inclination angle of $i = 65^\circ$ were used to derive all quantities, with the exception of CO for which we adopted $PA = 214^\circ$.

| Radius ($''$) | Radius (kpc) | $\Sigma_{*}^{3.6\mu\text{m}}$ ($M_\odot \text{ pc}^{-2}$) | $\Sigma_{*}^{4.5\mu\text{m}}$ ($M_\odot \text{ pc}^{-2}$) | Σ_{HI} ($M_\odot \text{ pc}^{-2}$) | Σ_{H_2} ($M_\odot \text{ pc}^{-2}$) |
|--------------------|-----------------|--|--|---|--|
| 10 | 0.20 | 79133.2 | 366294.1 | 5.34 | 239.8 |
| 20 | 0.41 | 13017.7 | 16754.8 | 5.85 | 237.3 |
| 30 | 0.61 | 4517.9 | 5203.2 | 6.17 | 189.1 |
| 40 | 0.81 | 2229.7 | 2452.3 | 6.09 | 168.5 |
| 50 | 1.02 | 1336.9 | 1406.3 | 5.72 | 97.5 |
| 60 | 1.22 | 972.2 | 995.5 | 5.32 | 104.2 |
| 70 | 1.43 | 729.9 | 742.1 | 5.29 | 72.5 |
| 80 | 1.63 | 592.1 | 599.7 | 5.17 | 53.9 |
| 90 | 1.83 | 496.0 | 500.9 | 5.52 | 38.4 |
| 100 | 2.04 | 428.7 | 429.8 | 5.69 | 43.0 |
| 110 | 2.24 | 379.3 | 379.8 | 5.59 | 33.9 |
| 120 | 2.44 | 339.8 | 342.9 | 5.32 | 29.7 |
| 130 | 2.65 | 309.2 | 310.5 | 5.24 | 23.8 |
| 140 | 2.85 | 274.6 | 277.0 | 4.99 | 14.4 |
| 150 | 3.05 | 249.6 | 251.1 | 4.87 | 12.4 |
| 160 | 3.26 | 218.4 | 219.9 | 4.97 | 13.1 |
| . | . | . | . | . | . |
| . | . | . | . | . | . |
| . | . | . | . | . | . |

Notes: Table 5 is published in its entirety in the electronic edition of *MNRAS*. A portion is shown here for guidance regarding its form and content.

8 STAR FORMATION

The interstellar medium (ISM) consists of dust, neutral gas and ionized gas, which are important ingredients to facilitate star formation (SF). As such, understanding the physical processes in the ISM and the star formation rate (SFR) are important to understand the physics of galaxy evolution and formation.

Despite the complexity of the ISM–SFR relationship, a widely used parameterized power-law between the SFR surface density, Σ_{SFR} , and the cold gas mass surface density, Σ_{gas} , in the form

$$\Sigma_{\text{SFR}} \propto \Sigma_{\text{gas}}^N, \quad (8)$$

has been introduced by Schmidt (1959). Later, observations and studies of a sample of spiral and starburst galaxies reveal a global correlation between the disk-averaged SFR and the gas mass surface density (e.g., Kennicutt 1998b; Kennicutt 1998a, and references therein), which is now known as the “Kennicutt-Schmidt law”, with a power-law index of $N = 1.4$. This measurement has been very useful as input to theoretical models of galaxy evolution (e.g., Kay et al. 2002).

8.1 The Global Star Formation Rate

Star formation mostly occurs in the nuclear region and inner spiral arms of galaxies. Some star formation also occurs in their outer disks (e.g., M83; Thilker et al. 2005; Koribalski et al. 2012, in prep.) and in interaction zones between galaxies (e.g., NGC 1512/1510 pair; Koribalski & López-Sánchez 2009). Traditionally, the UV stellar continuum and optical nebular recombination lines have been used as SFR indi-

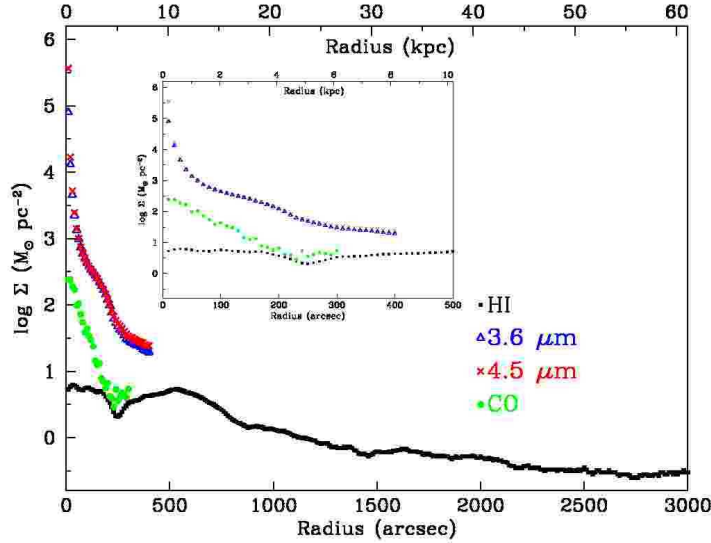


Figure 9. The stellar and gas mass surface densities of the Circinus Galaxy. The stellar component is derived from the IRAC 3.6 and 4.5 μm images (within the 1σ isophotal radius of $400''$) and the gaseous component from H I and CO(1–0) maps (see Table 5). The inset highlights our measurements at radii $< 500''$ (10 kpc).

cators but the former is severely affected by dust attenuation. On the other hand, MIR and FIR wavelengths are ideal to measure SFR due to UV photons from massive star formation absorbed by dust and re-radiated in these wavelengths. Numerous efforts to find SFR indicators related to MIR and FIR have been explored in the past decades (see e.g., Calzetti, Kinney & Storchi-Bergmann 1994; Kennicutt 1998b; Meurer, Heckman & Calzetti 1999; Salim et al. 2007). For an extensive review on the subject of deriving SFR relationship from measurements at MIR and FIR wavelengths, and their caveats, see Calzetti et al. (2007). Here we use a range of SFR relations to estimate the obscured global SFR of the Circinus Galaxy. A summary of the calculations is given in Table 6. We note that the PAH emission in the nuclear region is not related to the AGN as claimed in the NIR polarimetry study of the Circinus nucleus (Alexander, Ruiz & Hough 1999). We conclude that the obscured global SFR of the Circinus Galaxy is $\sim 3\text{--}8\text{ M}_{\odot}\text{ yr}^{-1}$.

In Figure 10 we show the global Kennicutt-Schmidt relation for a sample of nearby star forming galaxies Kennicutt (1998b). The calculated logarithmic Σ_{SFR} of the Circinus Galaxy is indicated by a red triangle; its value ($\sim 0.8\text{ M}_{\odot}\text{ yr}^{-1}\text{ kpc}^{-2}$) lies within the group of starburst galaxies.

8.2 The Local Star Formation Regions

Gas provides an excellent reservoir for fueling star formation activities. This is particularly prominent in high gas density regions. In this section, we present the first attempt in identifying local star forming regions in the Circinus Galaxy by using H I gas as a tracer. In Figure 11, we show a multi-wavelength color composite image of the Circinus Galaxy; two versions are shown: the first is showcases the IRAC imaging, 3.6 μm (blue) + 4.5 μm (green) + 8.0 μm (red), and the second consists of the high-resolution ATCA H I map

Table 6. Global star formation rates as derived from different calibration methods for the Circinus Galaxy.

| SFR ($\text{M}_{\odot}\text{ yr}^{-1}$) | Wavelength Required | Calibration Method | Ref. |
|--|------------------------|----------------------|------|
| 4.7 | 70 μm | L_{TIR} | (7) |
| 8.5 | 24 μm | $L_{\text{H}\alpha}$ | (1) |
| 6.7 | 8 μm | $L_{\text{H}\alpha}$ | (1) |
| 8.2 | 24 μm | $L_{1.4\text{GHz}}$ | (1) |
| 7.6 | 8 μm | $L_{1.4\text{GHz}}$ | (1) |
| 2.8 | 24 μm | $L_{24\mu\text{m}}$ | (2) |
| 4.3 | 24 μm | $L_{24\mu\text{m}}$ | (3) |
| 1.6 | 60 & 100 μm | L_{FIR} | (4) |
| 4.6 | 24 μm | $L_{24\mu\text{m}}$ | (5) |
| 0.7 ^a | 1.4 GHz | $L_{1.4\text{GHz}}$ | (6) |
| 3.5 ^b | 1.4 GHz | $L_{1.4\text{GHz}}$ | (6) |

Notes: ^a SFR for stellar masses $> 5\text{ M}_{\odot}$ and ^b for $> 0.1\text{ M}_{\odot}$. References: (1) Wu et al. (2005), (2) Calzetti et al. (2007), (3) Rieke et al. (2009), (4) Kennicutt (1998b), (5) Alonso-Herrero et al. (2006), (6) Condon, Cotton & Broderick (2002) and (7) Zhu et al. (2008).

(blue), the IRAC 8 μm map (red) and the IRAC 3.6 μm map (green). The physical size of the H I gas distribution extends well beyond the area shown here. The multi-wavelength composite images provide an powerful way to reveal the locations of star formation within the gaseous disk of Circinus.

In Figure 12, we overlay the high-resolution ATCA H I map in contours onto the IRAC 8 μm (left panel) and MIPS 24 μm (right panel) images. The contours start at H I gas column densities of $1.23 \times 10^{21}\text{ cm}^{-2}$. We identify 10 individual star forming regions in the IRAC 8 μm map that are clearly associated with high density H I gas. They are labeled according to their position with respect to the center of the Circinus Galaxy. The right panel shows the same H I contours overlaid onto the MIPS 24 μm image to highlight

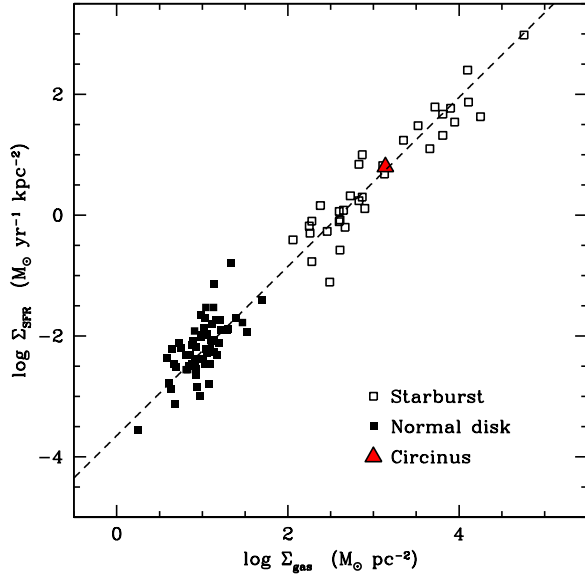


Figure 10. Global Kennicutt-Schmidt law (Kennicutt 1998b) for normal disk galaxies (filled squares) and starburst galaxies (open squares). The Circinus Galaxy is marked with a red triangle.

two resolved SF regions, C-1 and C-2, near the central region. For comparison we added CO(1–0) contours in grey; the map is rather small and has an angular resolution of $50''$ (Curran, Koribalski & Bains 2008). The higher resolution ($25''$) CO(2–1) map (not shown here) reveals molecular gas concentrations at the same location as the high-density H I clumps and clearly associated with the SF locations.

While there is generally a tight correlation between regions of high density gas and star formation activity (proportional to the MIR luminosity), we occasionally find exceptions (e.g., see Figure 13). Such mismatches have also been observed in other spiral galaxies (e.g., M83 bar transition region as explored in Jarrett et al. 2012). A ready explanation is related to the Lin–Shu density wave theory (Lin & Shu 1964, 1966), which was originally proposed to explain the spiral arm structure of galaxies. The idea suggests that the gas enters the density wave and is compressed due to enhanced gravity, which results in an increased local density. When the dense gas clouds reach the Jeans instability, they collapse to form new stars. As such, the local star formation rate in the region is also increased. Subsequently, the stars move out of the gas clouds, leaving the gas behind.

To evaluate if the mismatches follow the density wave theory prediction, we need to know the rotation direction of the Circinus Galaxy (clockwise or anti-clockwise). Based on the *Spitzer* composite image (see Figure 11 and the H I velocity field Jones et al. 1999) we conclude that Circinus rotates anti-clockwise, i.e., is co-rotating with the density wave. This implies the stars should form and lead ahead of the gas clumps in an anti-clockwise direction. This also applies for all SF regions. Examining all the mismatches, we conclude that most of them are consistent with the prediction.

Many studies are either supporting or confronting the density wave theory. We highlight a recent study by Foyle et al. (2011), in which multi-wavelength data of 12

nearby spiral galaxies have been used to calculate the angular cross-correlations in different star formation sequence. They conclude that the density wave theory is an oversimplification in explaining the spiral arm structure as seen in large disk galaxies.

9 COMPARISON BETWEEN 8 AND 24 MICRON EMISSION

A study by Bendo et al. (2008) has shown that the relation between the stellar continuum-subtracted PAH $8\ \mu\text{m}$ emission and $24\ \mu\text{m}$ hot dust emission exhibits a large scatter within the central 2 kpc of galaxies. Strong spatial variations of the (PAH $8\ \mu\text{m}$) / $24\ \mu\text{m}$ surface brightness ratio are also observed, with high values in the diffuse ISM and low values in bright star-forming regions. In order to study the (PAH $8\ \mu\text{m}$) / $24\ \mu\text{m}$ surface brightness ratio in Circinus, we prepared the data in a similar manner as described in Bendo et al. (2008). In the following we briefly describe the procedure and our results.

We first convolve the IRAC 3.6 and $8\ \mu\text{m}$ images to match the PSF of the MIPS $24\ \mu\text{m}$ image, which has a FWHM of $6''$. The convolution is necessary to allow a direct comparison of surface brightness within the same aperture in different wavebands. The IRAC 3.6 and $8\ \mu\text{m}$ images were then corrected for the diffusion of light through the IRAC detector. The effective aperture correction factors for these wavebands are listed in Section 4. Finally, we subtracted the stellar continuum from the IRAC $8\ \mu\text{m}$ and MIPS $24\ \mu\text{m}$ images using the equations derived by Helou et al. (2004)

$$I_{\text{PAH } 8\mu\text{m}} = I_{8\mu\text{m}} - 0.232 I_{3.6\mu\text{m}} \quad (9)$$

$$I_{24-3.6\mu\text{m}} = I_{24\mu\text{m}} - 0.032 I_{3.6\mu\text{m}}. \quad (10)$$

This results in a correction of about 30% and 2% to the 8 and $24\ \mu\text{m}$ surface brightness densities, respectively. Subsequently, we took the ratio of $I_{\text{PAH } 8\mu\text{m}}$ and $I_{24-3.6\mu\text{m}}$. Foreground stars, artifacts related to the bright galaxy core and low signal-to-noise areas ($<3\ \sigma$) were excluded from the analysis. The result is presented in Figure 14.

We find that the surface brightness ratio varies significantly across the disk of the Circinus Galaxy, with stronger point-like $24\ \mu\text{m}$ emission among the identified local star forming regions and with PAH $8\ \mu\text{m}$ emission dominating the diffuse ISM. The result is consistent with Bendo’s finding on other galaxies. In contrast, the PAH $8\ \mu\text{m}$ emission is dominant in the outer disk and along part of the spiral arms. The ratio variation of Circinus is similar to that of the nearby spiral galaxy NGC 3031 (see Figure 1 of Bendo et al. 2008).

10 SUMMARY AND CONCLUSIONS

We present a detailed study of the gas distribution and star formation activity in the inner and outer disk of the Circinus Galaxy. For this work, we utilized the infrared images obtained by the *Spitzer* IRAC and MIPS instruments, ATCA and Parkes H I radio data, as well as SEST CO maps. Due to the location of Circinus behind the Galactic Plane, removal of Milky Way stars and Galactic emission from the MIR images was necessary prior to further analysis. The detection

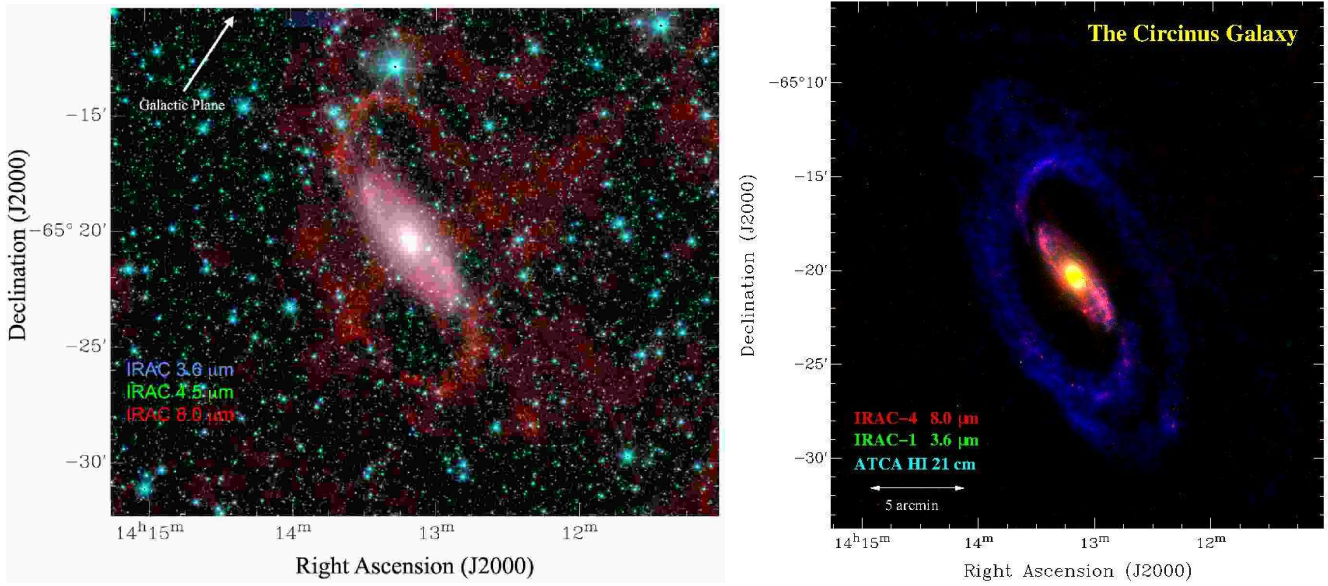


Figure 11. Multi-wavelength color-composite image of the Circinus Galaxy. **Left:** *Spitzer* IRAC combination: 8 μm (red), 4.5 μm (green), and 3.6 μm (blue) images. The large-scale Galactic emission and “spur” (Fig. 5) have been removed from the 8 μm image. **Right:** A combination of the high-resolution ATCA H I intensity map (blue) and the *Spitzer* IRAC 8 μm (red) and 3.6 μm (green) images, all three at a resolution of 15″.

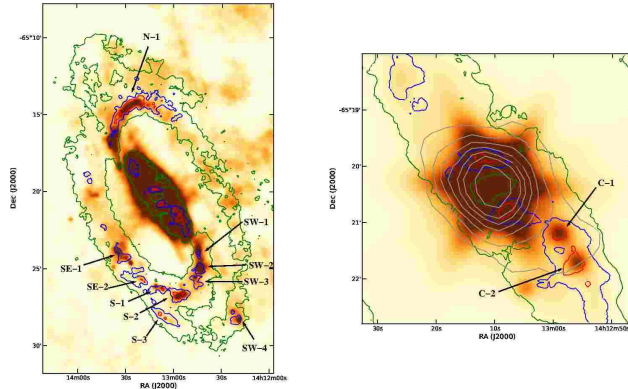


Figure 12. Comparison of H I, CO and mid-infrared emission in the inner disk of the Circinus Galaxy. The high-resolution ATCA H I intensity map (contours) is superimposed onto the calibrated and foreground-subtracted *Spitzer* IRAC 8.0 μm (left) and MIPS 24 μm (right) maps. Both *Spitzer* maps have been convolved to 15″ resolution to match the ATCA H I intensity map. The contour levels correspond to H I column densities, N_{HI} , of 1.23 (green), 2.45 (blue) and 3.19 (red) $\times 10^{21} \text{ cm}^{-2}$. CO(1–0) contours (grey) have been added to the *Spitzer* 24 μm map (right) which shows only the central region. The labels indicate local star forming regions as identified in Section 8.2.

and characterization tools developed by WDSC and IPAC successfully removed the MW stars in all *Spitzer* images. A correlation method and structure matching based on H I gas in different velocity ranges were used to remove both large- and small-scale foreground structure from the IRAC 8 μm and MIPS 24 μm images. We demonstrate that the single-dish and interferometer combined Galactic H I map can be used to remove the large-scale foreground Galactic ISM. Accordingly, a scaled high resolution Galactic H I map within a certain velocity range was used to remove the small-scale structure, notably the spur feature that, in projection, pierces the disk of the Circinus Galaxy. We confirm that the spur feature is related to the Galactic gas and with an esti-

mated distance of 5 kpc. A detailed description of removing the Galactic ISM is given in Section 3.2.

The physical properties via photometric analysis of the *Spitzer* images were determined for Circinus. Surface brightness profiles of Circinus in different 2MASS, IRAC and MIPS bands are shown in Figure 7. Using the spectral energy distribution, we derive a foreground visual extinction (A_V) of 2.1 mag toward the Circinus Galaxy, which is notably lower than the value implied by the extinction map of Schlegel, Finkbeiner & Davis (1998b). Stellar mass-to-light ratios in 3.6 μm and 4.5 μm bands were determined and utilized to infer the total stellar mass of $9.5 \times 10^{10} M_{\odot}$. The

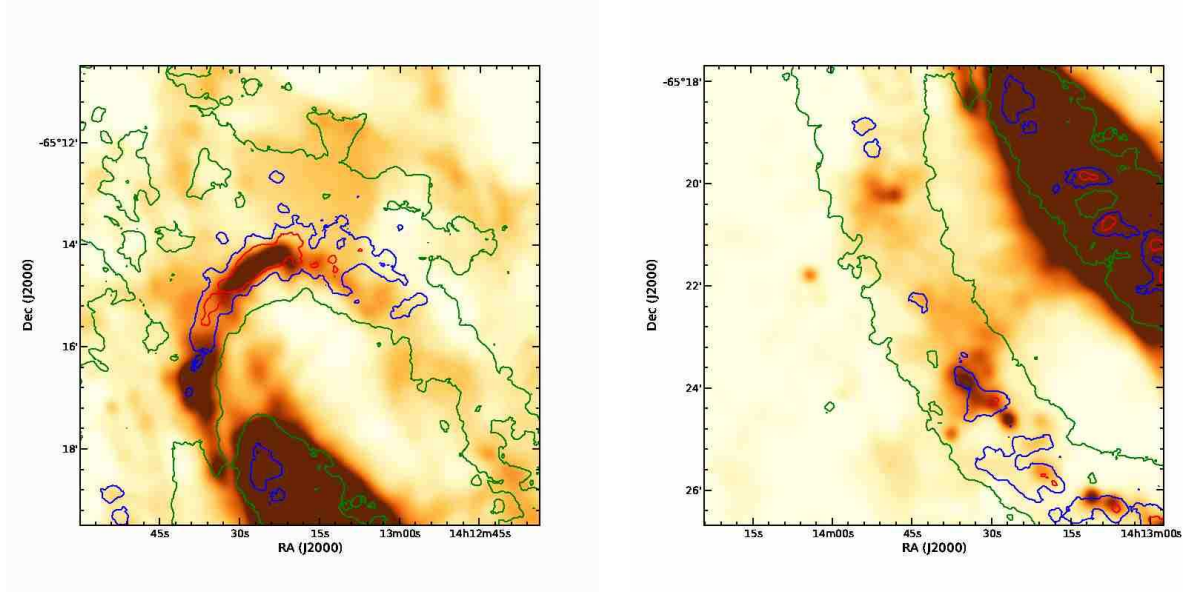


Figure 13. Comparison of ATCA H I and *Spitzer* 8 μm emission in the inner spiral arms of the Circinus Galaxy. Here we show an enlarged view of two different sections from Figure 12 (left panel). While bright star forming regions typically coincide with high density H I emission, faint star forming regions appear offset to H I enhancements.

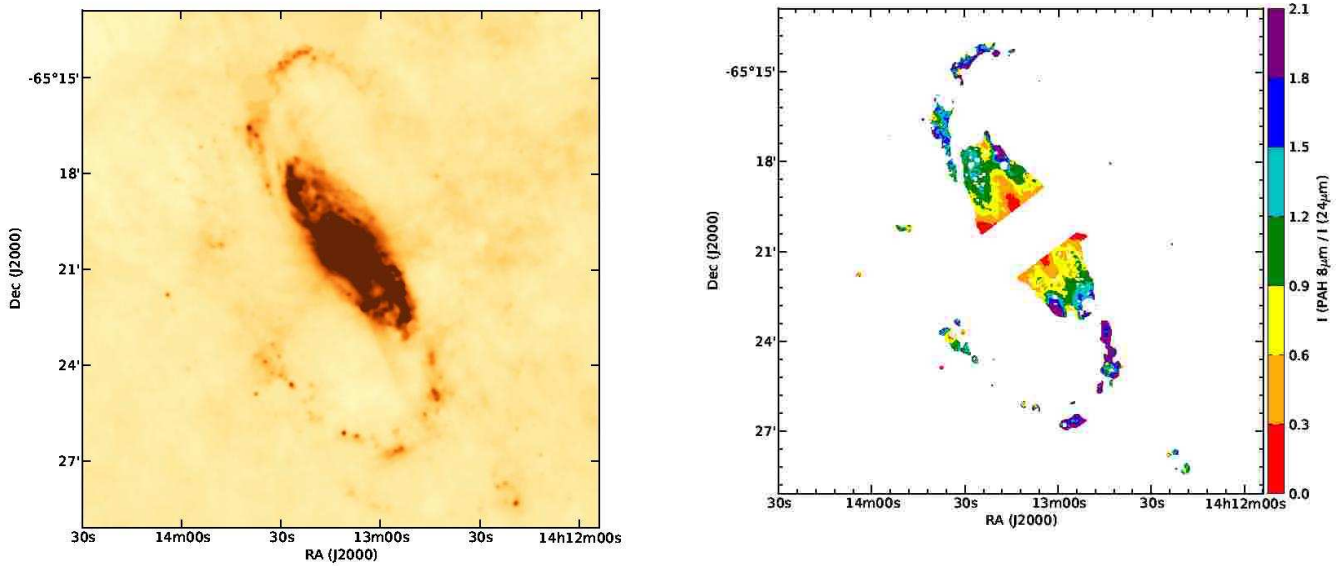


Figure 14. *Spitzer* 8 μm image (left) and stellar continuum-subtracted (PAH 8 μm) / 24 μm surface brightness ratio (right) of the Circinus Galaxy, both at an angular resolution of $6''$. The latter has been obtained following (Bendo et al. 2008); for comparison we use the same range for the ratio map. There is a clear color gradient from the center of Circinus to the edge of the inner disk and start of the spiral arms. Artifacts affected by the bright core and foreground stars have been removed. The red color in the ratio map corresponds to relatively weak emission from PAH 8 μm while blue indicates strong PAH emission.

sum of neutral hydrogen and molecular hydrogen masses gives a total gas mass of $9 \times 10^9 M_{\odot}$ for Circinus.

Using various wavelength calibrations, we derived the obscured star formation rates of the Circinus Galaxy between 3 and $8 M_{\odot} \text{ yr}^{-1}$. The star formation surface density follows the Kennicutt-Schmidt law and the value is similar to other starburst galaxies. Multiwavelength color composite

images of Circinus as shown in Figure 11 reveal the prominent spiral arm, inner and outer disk. The H I gas traces the PAH 8 μm feature, which strongly correlates with the local star forming regions. Cross-correlating the IRAC 8 μ and MIPS 24 μm images with the high-resolution ATCA H I map, we identified 12 distinct/resolved individual star forming regions. One of the star formation regions (SW-4)

is located in the outskirt of Circinus. We also identified several offsets between the gas clumps and stars in Circinus. Analysis of these offsets supports the density wave scenario. However, a different scenario is likely needed to explain several anti-correlated exceptions.

Finally, we compared the PAH 8 μm and 24 μm dust emission and found a significant variation across the disk of Circinus. Enhanced 24 μm emission relative to PAH 8 μm emission was also found in identified local star forming regions.

ACKNOWLEDGMENTS

B.-Q. For is the recipient of a John Stocker Postdoctoral Fellowship from Australia's Science and Industry Endowment Fund (SIEF). She thanks the generous travel support to Australia from the University of Texas astronomy department Cox Excellence fund and the financial support by CSIRO Astronomy and Space Science during summer 2010. We also thank Michelle Cluver and Tobias Westmeier for helpful discussions. This work is based [in part] on observations made with the *Spitzer* and research using the NASA/IPAC Extragalactic Database (NED) and IPAC Infrared Science Archive, all are operated by JPL, Caltech under a contract with the National Aeronautics and Space Administration. Support for this work was provided by NASA through an award issued by JPL/Caltech.

REFERENCES

- Alexander D. M., Ruiz M., Hough J. H., 1999, in ESA Special Publication, Vol. 435, Workshop on ISO Polarisation Observations, R. J. Laureijs & R. Siebenmorgen, ed., p. 1
- Alonso-Herrero A., Rieke G. H., Rieke M. J., Colina L., Pérez-González P. G., Ryder S. D., 2006, *ApJ*, 650, 835
- Arce H. G., Goodman A. A., 1999, *ApJL*, 512, L135
- Bauer F. E., Brandt W. N., Sambruna R. M., Chartas G., Garmire G. P., Kaspi S., Netzer H., 2001, *AJ*, 122, 182
- Bell E. F., de Jong R. S., 2001, *ApJ*, 550, 212
- Bendo G. J. et al., 2008, *MNRAS*, 389, 629
- Bloemen J. B. G. M. et al., 1986, *A&A*, 154, 25
- Broeils A. H., van Woerden H., 1994, *A&A Supp.*, 107, 129
- Calzetti D., Kennicutt R. C., Engelbracht C. W., Leitherer C., Draine B. T., Kewley L., Moustakas J., 2007, *ApJ*, 666, 870
- Calzetti D., Kinney A. L., Storchi-Bergmann T., 1994, *ApJ*, 429, 582
- Cardelli J. A., Clayton G. C., Mathis J. S., 1989, *ApJ*, 345, 245
- Condon J. J., Cotton W. D., Broderick J. J., 2002, *AJ*, 124, 675
- Curran S. J., Koribalski B. S., Bains I., 2008, *MNRAS*, 389, 63
- Cutri R. M. et al., 2011, Explanatory Supplement to the WISE Preliminary Data Release Products. Tech. rep., IPAC/California Institute of Technology
- Draine B. T., Li A., 2007, *ApJ*, 657, 810
- Elmouttie M., Koribalski B., Gordon S., Taylor K., Houghton S., Lavezzi T., Haynes R., Jones K., 1998, *MNRAS*, 297, 49
- Foyle K., Rix H.-W., Dobbs C. L., Leroy A. K., Walter F., 2011, *ApJ*, 735, 101
- Freeman K. C., Karlsson B., Lynga G., Burrell J. F., van Woerden H., Goss W. M., Mebold U., 1977, *A&A*, 55, 445
- Gardner F. F., Whiteoak J. B., 1982, *MNRAS*, 201, 13P
- Ghosh S. K., Bisht R. S., Iyengar K. V. K., Rengarajan T. N., Tandon S. N., Verma R. P., 1992, *ApJ*, 391, 111
- Helou G. et al., 2004, *ApJS*, 154, 253
- Henning P. A. et al., 2000, *AJ*, 119, 2686
- Hunter S. D. et al., 1997, *ApJ*, 481, 205
- Jarrett T. H., Chester T., Cutri R., Schneider S. E., Huchra J. P., 2003, *AJ*, 125, 525
- Johnston S., Koribalski B., Weisberg J. M., Wilson W., 1996, *MNRAS*, 279, 661
- Jones K. L., Koribalski B. S., Elmouttie M., Haynes R. F., 1999, *MNRAS*, 302, 649
- Kalberla P. M. W. et al., 2010, *A&A*, 521, A17
- Kay S. T., Pearce F. R., Frenk C. S., Jenkins A., 2002, *MNRAS*, 330, 113
- Kennicutt, Jr. R. C., 1998a, *ARA&A*, 36, 189
- , 1998b, *ApJ*, 498, 541
- Kohyama T., Shibai H., Fukagawa M., Hibi Y., 2010, *ApJ*, 719, 873
- Koribalski B., 1996, in Astronomical Society of the Pacific Conference Series, Vol. 106, The Minnesota Lectures on Extragalactic Neutral Hydrogen, E. D. Skillman, ed., p. 238
- Koribalski B. S., 2008, in *Galaxies in the Local Volume*, Koribalski, B. S. & Jerjen, H., ed., Springer, p. 41
- Koribalski B. S., López-Sánchez Á. R., 2009, *MNRAS*, 400, 1749
- Koribalski B. S. et al., 2004, *AJ*, 128, 16
- Li A., Draine B. T., 2001, *ApJ*, 554, 778
- Lin C. C., Shu F. H., 1964, *ApJ*, 140, 646
- , 1966, *Proceedings of the National Academy of Science*, 55, 229
- López-Sánchez Á. R., Koribalski B. S., van Eymeren J., Esteban C., Kirby E., Jerjen H., Lonsdale N., 2012, *MNRAS*, 419, 1051
- Marconi A., Moorwood A. F. M., Origlia L., Oliva E., 1994, *The Messenger*, 78, 20
- Marsh K. A., Jarrett T. H., 2012, *PASA Special Issue*, in press
- Matt G. et al., 1996, *MNRAS*, 281, L69
- McCallum J. N., Ellingsen S. P., Lovell J. E. J., Phillips C. J., Reynolds J. E., 2009, *MNRAS*, 392, 1339
- McClure-Griffiths N. M. et al., 2009, *ApJS*, 181, 398
- Mebold U., Goss W. M., Freeman K. C., van Woerden H., 1976, *Proceedings of the Astronomical Society of Australia*, 3, 72
- Meurer G. R., Heckman T. M., Calzetti D., 1999, *ApJ*, 521, 64
- Moorwood A. F. M., Lutz D., Oliva E., Marconi A., Netzer H., Genzel R., Sturm E., de Graauw T., 1996, *A&A*, 315, L109
- Oh S., de Blok W. J. G., Walter F., Brinks E., Kennicutt R. C., 2008, *AJ*, 136, 2761
- Oliva E., Marconi A., Cimatti A., Alighieri S. D. S., 1998, *A&A*, 329, L21
- Oliva E., Salvati M., Moorwood A. F. M., Marconi A., 1994, *A&A*, 288, 457
- Polletta M. et al., 2007, *ApJ*, 663, 81

- Reach W. T. et al., 2005, *PASP*, 117, 978
- Rieke G. H., Alonso-Herrero A., Weiner B. J., Pérez-González P. G., Blaylock M., Donley J. L., Marcillac D., 2009, *ApJ*, 692, 556
- Salim S. et al., 2007, *ApJS*, 173, 267
- Sault R. J., Teuben P. J., Wright M. C. H., 1995, in *Astronomical Society of the Pacific Conference Series*, Vol. 77, *Astronomical Data Analysis Software and Systems IV*, R. A. Shaw, H. E. Payne, & J. J. E. Hayes, ed., p. 433
- Schlegel D. J., Finkbeiner D. P., Davis M., 1998a, *ApJ*, 500, 525
- , 1998b, *ApJ*, 500, 525
- Schmidt M., 1959, *ApJ*, 129, 243
- Silva L., Granato G. L., Bressan A., Danese L., 1998, *ApJ*, 509, 103
- Solomon P. M., Rivolo A. R., Barrett J., Yahil A., 1987, *ApJ*, 319, 730
- Stanimirovic S., 2002, in *Astronomical Society of the Pacific Conference Series*, Vol. 278, *Single-Dish Radio Astronomy: Techniques and Applications*, S. Stanimirovic, D. Altschuler, P. Goldsmith, & C. Salter, ed., pp. 375–396
- Steer D. G., Dewdney P. E., Ito M. R., 1984, *A&A*, 137, 159
- Strong A. W. et al., 1988, *A&A*, 207, 1
- Thilker D. A. et al., 2005, *ApJL*, 619, L79
- Tully R. B., Rizzi L., Shaya E. J., Courtois H. M., Makarov D. I., Jacobs B. A., 2009, *AJ*, 138, 323
- Westmeier T., Braun R., Koribalski B. S., 2011, *MNRAS*, 410, 2217
- Whiteoak J. B., Gardner F. F., 1986, *MNRAS*, 222, 513
- Wilson W. E. et al., 2011, *MNRAS*, 416, 832
- Wu H., Cao C., Hao C., Liu F., Wang J., Xia X., Deng Z., Young C., 2005, *ApJL*, 632, L79
- Zhu Y.-N., Wu H., Cao C., Li H.-N., 2008, *ApJ*, 686, 155